Journal of the Meteorological Society of Japan

EARLY ONLINE RELEASE

The DOI for this manuscript is

DOI:10.2151/jmsj.2021-032

J-STAGE Advance published date: January 21st, 2021

The final manuscript after publication will replace the preliminary version at the above DOI once it is available.

Vertical Evolution of Microphysical Properties during Snow Events in Middle Latitudes of China Observed by a C-band Vertically Pointing Radar

Ye Cui

Collaborative Innovation Center on Forecast and Evaluation of Meteorological Disasters, NUIST, Nanjing, China and State Key Laboratory of Severe Weather, Chinese Academy of Meteorological Sciences, Beijing, China

Zheng Ruan

State Key Laboratory of Severe Weather, Chinese Academy of Meteorological Sciences, Beijing, China

Ming Wei

Collaborative Innovation Center on Forecast and Evaluation of Meteorological Disasters, NUIST, Nanjing, China

Feng Li, Runsheng Ge

State Key Laboratory of Severe Weather, Chinese Academy of Meteorological Sciences, Beijing, China

Yong Huang

Atmospheric Science and Satellite Remote Sensing Anhui Province Key Lab

Corresponding author address: Zheng Ruan, State Key Lab of Severe Weather, Chinese Academy of Meteorological Sciences, 46 Zhongguancun South Avenue, Beijing, China.

E-mail: ruanz@cma.gov.cn

ABSTRACT

This study applied the C-band vertically pointing radar with frequency-modulation continuous-wave technology to obtain the continuous observation data of four shallow and two deep snow events during the winter of 2015–2016 in the midlatitudes of China. Generating cells (GCs) were found near the echo tops in every event. The ice particle number concentration (N), ice water content (IWC), and median mass diameter (D_m) retrieved from radar Doppler spectra were used to analyze the microphysical properties in the snow clouds. The clouds were divided into upper GC and lower stratiform (St) regions according to their vertical structure. The fall streaks (FSs) associated with GCs were embedded in the St regions. In the GC regions, the N values in shallow events were smaller compared with deep events, while D_m and IWC were larger. In the St regions, N decreased compared with the GC regions, while the D_m and IWC increased, implying the existence of aggregation and deposition growth. The growth of particle size and mass mainly occurred in the St regions. The increases of N were usually observed near −5°C accompanied by bimodal Doppler spectra, which might be caused by ice multiplication. The average ratios of the median N, D_m, and IWC inside GCs to those outside GCs are 2, 1.3, and 2.5 respectively for shallow events, with 1.7, 1.2, and 2.3 respectively for deep events. These values were basically the same as those for the FSs, implying the importance of GCs to the enhanced ice growth subsequently found in FSs. The larger values of N, D_m, and IWC inside GCs could be related to the upward air motions inside GCs. The first Z_e–IWC relationship suitable for snow clouds in the midlatitudes of China was also

established.

1. Introduction

The generating cells (GCs) and associated fall streaks (FSs) were observed and studied in a variety of environments from the 1950s (e.g., Marshall 1953; Gunn et al. 1954; Henrion et al. 1978; Sienkiewicz et al. 1989; Syrett et al. 1995; Wolde and Vali 2002; McFarquhar et al. 2011; Cunningham and Yuter 2014; Kumjian et al. 2014). The term GC describes a small region of locally high radar reflectivity at the cloud top from which an enhanced reflectivity trail characteristic of falling snow particles originates (American Meteorological Society 2016). The trails embedded in the stratiform clouds are termed FSs with patterns often shown as virga-like slanted streaks. The GCs seem significant in the formation of precipitation (e.g., Douglas et al. 1957; Rutledge and Hobbs 1983).

Early studies (e.g., Marshall 1953; Gunn et al. 1954; Wexler 1955; Boucher 1959) observed GCs near the cloud top by using vertically pointing radars. The horizontal extent of GCs was approximately 1.6 km (Langleben 1956), and the updraft velocities in GCs were derived between 0.75 and 3 m s^{-1} (Wexler and Atlas 1959). Subsequently, Doppler radars were also introduced to GC research. Carbone and Bohne (1975) estimated that the maximum vertical air velocities in GCs were about ±1.5 m s^{-1}.

During the cyclonic extratropical storms program in the late 1970s and early 1980s, vertically pointing Doppler radar observations of GCs at the tops of warm- and occluded-frontal clouds largely supported the early findings from the 1950s (e.g., Hobbs and Locatelli 1978; Herzegh and Hobbs 1980; Houze et al. 1981). Houze et al. (1981) assumed that there were enhanced nucleation and initial particle growth in GCs. They also reported that about 80% of the particle mass growth occurred below the GC level. The deposition was the predominant ice-growth mechanism in GCs, and the particles below grew by deposition and aggregation.

During the 2009–2010 profiling of winter storms (PLOWS) project, by using the data detected by airborne Wyoming cloud radar, Rosenow et al. (2014) made a statistical analysis on the structure and vertical velocity of GCs. They found that GCs were usually 1–2 km deep, with a horizontal extent of 0.5–2 km and vertical air velocities of 1–2 $\mathrm{m\,s^{-1}}$. Plummer et al. (2014) analyzed data obtained by airborne cloud radar and lidar and a suite of in situ microphysical probes statistically. They found that ice particle number concentrations (N) averaged 1.9 times larger inside GCs compared to outside, and ice water contents (IWC) and median mass diameters (D_{m}) averaged 2.2 and 1.1 times larger inside GCs, respectively. They also observed that riming existed in the GC regions. By statistical analysis on the microphysical characteristics of FSs, Plummer et al. (2015) presented that the values of N, IWC, and D_{m} were enhanced inside FSs compared to outside, and the enhancements between the inside and outside of FSs were similar to those of GCs. They also found that the growth mechanism of ice particles was similar between the inside and outside of FSs, and the ice growth by deposition and aggregation mainly occurred below the GC level.

The polarimetric radars were also used in GC and FS research. Kumjian et al. (2014)

observed 19 snowstorms over northern Colorado by using the high-resolution X-band polarimetric radar. They found that aggregation and riming could exist in the core of GCs. Keppas et al. (2018) analyzed the structure, origin, and effects of FSs embedded in warm fronts through the data detected by polarimetric radar and airborne microphysical probes. In situ detection is the most intuitive way to understand GCs and FSs, but the in situ measurements of GCs and FSs are limited. Furthermore, the data obtained by airborne instruments lack continuity and integrity. The studies about continuous microphysical processes occurring inside and outside GCs and FSs are uncommon.

Compared with pulsed radars, radars equipped with frequency-modulation continuous-wave (FMCW) technology have several advantages such as more precise distance and velocity measurements, higher spatial and temporal resolution, lower transmitting peak power, and higher reliability. Therefore, FMCW technology can realize more detailed detection of cloud and precipitation targets. The Chinese Academy of Meteorological Sciences developed the C-band vertically pointing radar with FMCW (CVPR-FMCW) technology in 2013, which was used to detect precipitation clouds. Cui et al. (2020) (hereafter C20) analyzed vertical structure and dynamical properties of six snow events in Shou County (a typical region in the midlatitudes of China) during the winter of 2015–2016 using CVPR-FMCW. On this basis, this study will retrieve and analyze the microphysical properties of the same six snow events.

The next section summarizes the instrumentation and data. In Section 3, the method of retrieving microphysical parameters by radar Doppler spectra is described in detail. In Section 4, the six snow events are classified into deep and shallow categories, and the snow clouds are divided into GC regions and stratiform regions (St regions) for case studies and statistical analysis. The establishment of Z_e–IWC relationship and error discussion are also presented in Section 4. Finally, Section 5 provides the conclusions of this study.

2. Instrumentation and Data

Since the instrumentation and data used in this study are the same as those described in C20, only a brief summary is provided here. This study requires the vertical air velocity (W_a) retrieved in C20, so the related part will also be summarized here.

The CVPR-FMCW, located at the meteorological station in Shou County (32°26′N, 116°47′E) has high spatial and temporal resolution (30 m and 3 s, respectively), with the velocity resolution of 0.0895 m s^{-1}. The maximum usable range of the CVPR-FMCW is 15–24 km and the minimum measurable signal power is close to −170 dBm to capture the extremely weak signals. The radar outputs power spectral density distribution with 512 channels, which can be converted into the reflectivity spectral density distribution via the radar equation, allowing the calculation of three spectral parameters (reflectivity, radial velocity, and spectral width).

The Doppler spectra of ground-based vertically pointing radars provide abundant information for understanding the dynamical and microphysical processes in clouds.

Cui et al. (2020) used the Doppler spectra combined with reflectivity (Z) and radial velocity (V_r) during six snow events obtained by CVPR-FMCW to understand the vertical structure of snow clouds and retrieve the W_a in the clouds. According to the echo top height of the snow clouds, the six snow events during the winter of 2015–2016 were classified into two types, namely deep (>10 km) and shallow (<8 km). Between the deep and shallow events, both temperatures and depths of the GC regions were distinctly different, and the growth rates of Z in the GC regions were also different. According to the vertical distribution characteristics of Z, V_r, and their vertical gradients, the clouds were divided into upper GC and lower St regions. In C20, bimodal Doppler spectra were used to establish the relationships between Z and the reflectivity-weighted particle fall speed (V_z) for the two regions in two types of snow events. The V_z was then retrieved and corrected for air density and the W_a was calculated by V_r minus V_z. Therefore, the understanding of dynamical characteristics in the clouds was obtained. Since V_z is very close to the terminal fall speed of particles (V_t) (Ralph 1995), the V_z retrieved by C20 is regarded as V_t in this study. The information of the six snow events is summarized in Table 1. Different from C20, the ranges of temperature (T) and relative humidity with respect to ice (RH_i) are for the whole snow clouds.

Many studies used the correlation of Z–V_t relationships to determine the types of ice particles (e.g., Kalesse et al. 2013; Protat and Williams 2011; Straka et al. 2000), and the ice particle types of two regions in two types of snow events were also preliminarily identified in C20 by this method. The hexagonal plates were identified to be the main particle type in the GC regions of shallow events, since the Z–V_t relationship established for these regions was very close to the Z–V_t relationship for hexagonal plates. For the same reason, C20 considered that the GC regions of deep events were mainly composed of bullet rosettes, and the St regions in the two types of snow events were mainly composed of aggregates. The deduced particle types in GC and St regions are consistent with those observed by Plummer et al. (2014) and Plummer et al. (2015), respectively. Based on the main ice particle types identified in C20, this study will retrieve and analyze the microphysical parameters (N, D_m, and IWC) in the snow clouds.

Table 1: The information of the six snow events.

Event type	Date	Snow periods	Range of T (°C)	Range of RH_i (%)	Average cloud top (km)
Shallow	27 Jan 2015	0032UTC–0430UTC	−21 to −1	65–148	5.2
	28 Jan 2015	0000UTC–1200UTC	−27 to 0	80–150	7.3
	29 Jan 2015	0020UTC–1151UTC	−25 to −2	74–142	6.2
	20 Jan 2016	1230UTC–1600UTC	−20 to 0	67–140	5.3
Deep	28 Feb 2015	0000UTC–0335UTC	−62 to 0	90–140	11.2
	24 Nov 2015	0855UTC–1200UTC	−59 to −1	86–141	11.1

Since there is no radiosonde at the Shou County meteorological station, this study still uses the sounding data of Fuyang meteorological station (about 95 km northwest of Shou County) to analyze the atmospheric temperature and humidity conditions, as described in C20. During the winter, mid- and upper-level winds generally come from the northwest. Because Fuyang lies to the northwest of Shou County, the weather conditions of Fuyang and Shou County are similar. The typical deep (28 February 2015) and shallow (20 January 2016) events are selected, as described in C20. Figure 1 shows the T profiles and relative humidity (RH) profiles made by air sounding data (recorded per second) near the snow periods.

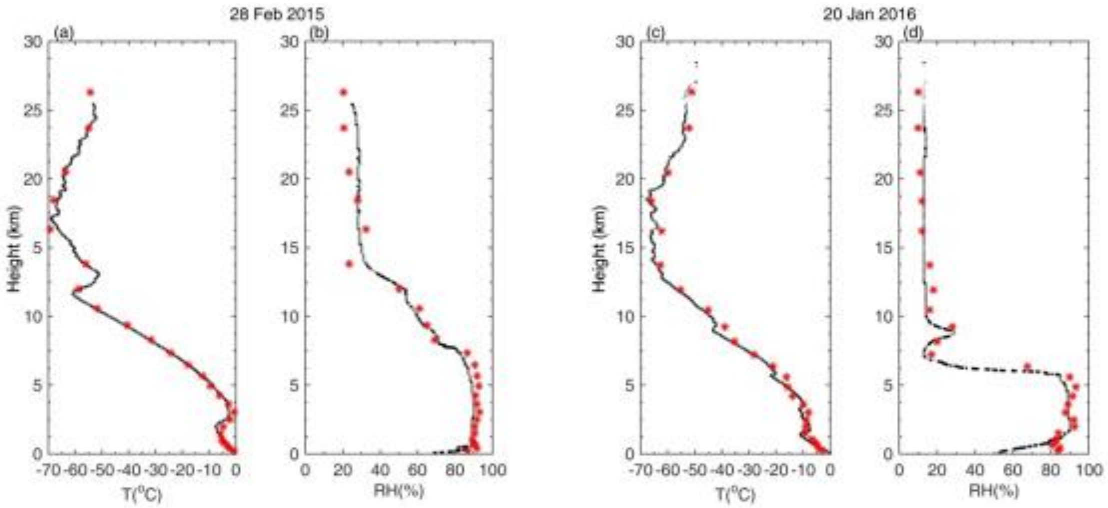

Fig. 1. The *T* and RH profiles on (a) and (b) 0000 UTC 28 Feb 2015, (c) and (d) 1200 UTC 20 Jan 2016, at Fuyang radiosonde station. The red asterisks represent the ERA5 data over Shou County at the corresponding time.

Because of the close relationship between microphysical processes and atmospheric conditions, we obtained the fifth generation atmospheric reanalysis data from the European Center for Medium-Range Weather Forecasts (ERA5) over Shou County to compare it with the air sounding data of the Fuyang meteorological station. Figure 1 shows the ERA5 data as the red asterisks. As shown in Fig. 1, the ERA5 data were close to the air sounding profiles, and the air sounding data points were much more than the ERA5 data, so that the variation of atmospheric temperature and humidity reflected by air sounding data was more detailed. Therefore, the following sections will analyze the microphysical processes by using air sounding data.

3. Retrieving microphysical parameters by radar Doppler spectra

The radar Doppler spectra contain both the scattering intensity information and the velocity information of particles in the clouds. When a radar vertically detects snow clouds, the power spectral density distribution of particles within the sampled volume at altitude h is named $S_h(V_r)$. Through the radar equation, $S_h(V_r)$ can be converted into the equivalent reflectivity spectral density distribution named $Z_{eh}(V_r)$, where Z_e is used instead of Z to represent the non-Rayleigh scattering. As described in Section 2, V_r minus W_a can be considered as V_t. The W_a was retrieved in C20, so that $Z_{eh}(V_r)$ can be converted into equivalent reflectivity spectral density distribution under the condition of static atmosphere named $Z_{eh}(V_t)$ after removing the influence of W_a on the detected fall speeds of particles. The reflectivity spectral density distribution in discrete form is composed of multiple spectral lines. The relationship between the equivalent reflectivity at height h ($Z_e(h)$) and the equivalent reflectivity at a single spectral line within the corresponding range gate ($Z_{ehi}(V_t)$) is shown as Eq. (1):

$$Z_e(h) = \sum_{i=-N_{FFT}/2}^{i=N_{FFT}/2} Z_{ehi}(V_t)\Delta v \quad (i=0,1,2\ldots N_{FFT}) \qquad (1)$$

where Δv is the interval between two adjacent spectral lines, with the value of 0.0895 m s^{-1}, and N_{FFT} is the number of spectral lines, with the value of 512.

Since the calculation of Z_e is closely related to particle size (D), it is necessary to convert $Z_{ehi}(V_t)$ into the equivalent reflectivity of a single spectral line with D being the independent variable ($Z_{ehi}(D)$). Note that particle size in this study means the maximum dimension of the particle. The equivalent reflectivity of the ith spectral line can be expressed by Eq. (2):

$$Z_{ehi}(D_i) = C \cdot N_{hi}(D_i) \cdot \sigma(D_i) \cdot \Delta D \qquad (2)$$

where $C = 10^6\lambda^4/\pi^5/|K|^2$, λ is wavelength with the unit of cm, D_i is the particle maximum dimension of the ith spectral line with the unit of cm, $N_{hi}(D_i)$ is the particle number density of the ith spectral line with the unit of $m^{-3}\,cm^{-1}$, and $\sigma(D_i)$ is the backscattering cross-section of a single particle with the unit of cm^2. The dimensionless quantity K is the Clausius-Mossotti factor of liquid water that can be calculated by the complex refraction index of liquid water (m), $K = (m^2 - 1)/(m^2 + 2)$.

Thus, if the $Z_{ehi}(V_t)$ is known, the V_t–D relationship and $\sigma(D)$ are required to calculate $N_{hi}(D)$, which are described in Section 3.1 and 3.2, respectively. The sum of $N_{hi}(D)$ of each spectral line in a range gate is the N at the corresponding height.

Moreover, D_m and IWC are also retrieved in this study. The IWC corresponding to a single spectral line is expressed by Eq. (3):

$$IWC_{hi}\left(D_i\right) = m(D_i) \cdot N_{hi}\left(D_i\right) \cdot \Delta D \qquad (3)$$

where $m(D_i)$ is the mass of a single particle with the size of D_i. The sum of $IWC_{hi}(D_i)$ of each spectral line in a range gate is the IWC at the corresponding height. According to Eq. (3), the m–D relationship is indispensable for calculating the IWC, which is described in Section 3.1.

The calculation expression of D_m at a certain height (Delanoë et al. 2007) is shown as Eq. (4):

$$D_m = \frac{\sum_{i=-N_{FFT}/2}^{i=N_{FFT}/2} N_{hi}\left(D_i\right) D_i^4 \Delta D}{\sum_{i=-N_{FFT}/2}^{i=N_{FFT}/2} N_{hi}\left(D_i\right) D_i^3 \Delta D} \qquad (\mathrm{i}=0,1,2\ldots N_{FFT}) \qquad (4)$$

In conclusion, the key problems of retrieving N, IWC, and D_m are finding a reasonable V_t–D and m–D relationships, and calculating the backscattering cross-section of ice particles (σ).

3.1. V_t–D and m–D relationships

During the 1970s and 1980s, some studies used experimental data and approximate theories to establish empirical relationships to calculate the V_t of ice particles with a given shape, size, and mass. These relationships usually have the following form:

$$V_t = aD^b \qquad (5)$$

where D is the maximum dimension of the particle; the constants a and b were measured from a variety of particle habits (e.g., Locatelli and Hobbs 1974; Kajikawa 1982).

However, these relationships are only appropriate for specific cases. For similar particles, the differences among relationships obtained from different studies are significant. Therefore, a more general aerodynamic method (e.g., Mitchell 1996; Heymsfield and Westbrook 2010) was selected to obtain the V_t–D relationship.

The fall speeds of solid particles are related to their shape, volume density, and air density. In general, the drag on a falling particle can be expressed by a dimensionless drag coefficient C_d:

$$F_d = \frac{1}{2}\rho_{air} V_t^2 A C_d \qquad (6)$$

where ρ_{air} is the air density, F_d is the drag force, and A is the projected area. In general, C_d is a function of the Reynolds number Re, which can be expressed as $\mathrm{Re} = \rho_{air} V_t D/\eta$, where η is the dynamic viscosity of the air. To facilitate the calculation of V_t, the Best number $X = C_d \mathrm{Re}^2$ is introduced. When the F_d in Eq. (6) is equal to the weight of the particle mg, where g is gravity, the following results can be obtained:

$$X = \frac{\rho_{air}}{\eta^2}\frac{2mgD^2}{A} \qquad (7)$$

The area ratio of the particle A_r is introduced, defined as the ratio of the particle's projected area A to the area of a circumscribing circle, $A_r = A/[(\pi/4)D^2]$. Substitution into Eq. (7) yields:

$$X = \frac{\rho_{air}}{\eta^2}\frac{8mg}{\pi A_r} \qquad (8)$$

To adjust the calculation sensitivity of V_t related to A_r, Heymsfield and Westbrook (2010) improved X to a modified Best number X^*:

$$X^* = \frac{\rho_{air}}{\eta^2}\frac{8mg}{\pi A_r^{0.5}} \qquad (9)$$

After calculating X^*, Re can also be estimated according to the relationship between X^* and Re, as shown in Eq. (10):

$$\mathrm{Re} = \frac{\delta_0^2}{4}\left[\left(1+\frac{4\sqrt{X^*}}{\delta_0^2\sqrt{C_0}}\right)^{1/2}-1\right]^2 \qquad (10)$$

where C_0 is the inviscid drag coefficient with a value of 0.35, and δ_0 is a dimensionless coefficient with a value of 8.0.

Finally, the V_t can be computed by the following equation:

$$V_t = \eta\,\mathrm{Re}/D\rho_{air} \qquad (11)$$

According to Eq. (9), estimating m and A by the power-law m–D and A–D relationships of ice particles with different shapes is necessary to calculate X^*. The forms of the above two relationships are $m = \alpha D^{\tau}$ and $A = \omega D^{\theta}$, respectively. As explained in Section 2, the particle types required in this study are hexagonal plates, bullet rosettes, and aggregates. During the deep events, the T within the snow clouds was from about −60°C to 0°C as shown in Table 1. Although the GC regions were mainly classified as bullet rosettes, columnar and plate-like ice crystals would also exist as the T increased. Therefore, the aggregates of plates, columns, and bullets were regarded as the dominant particle type in the St regions of the deep events. During the shallow events, the T within the snow clouds was from −20°C to 0°C (Table 1). Columns and bullets are rarely seen in this temperature range (Bailey and Hallett 2009); therefore, the aggregates of plates were regarded as the dominant particle type in the St regions of the shallow events. Table 2 shows the parameters corresponding to different types of ice particles (Mitchell 1996). According to Mitchell (1996), the parameters are different for different ranges of particle size. To select the appropriate parameters, the ranges of particle size were estimated roughly by the retrieved V_t (C20) and the V_t–D relationships from Locatelli and Hobbs (1974) and Matrosov and Heymsfield (2000). Note that the units of m, A, and D are g, cm^2, and cm respectively, when m and A are calculated by the power law m–D and A–D relationships.

Table 2. The parameters in the power law m–D and A–D relationships corresponding to different types of ice particles.

Related region	Particle type	α	τ	ω	θ
GC region of shallow events	Hexagonal plates 100μm<D≤3000μm	0.00739	2.45	0.65	2.00
GC region of deep events	Bullet rosettes 200μm≤D≤1000μm	0.00308	2.26	0.0869	1.57
St region of shallow events	Aggregates of plates 600μm≤D≤4100μm	0.0033	2.2	0.2285	1.88
St region of deep events	Aggregates of plates columns and bullets	0.0028	2.1	0.2285	1.88

(800μm≤D≤4500μm)

3.2. The calculation of σ

Because of the complex shapes of ice particles, the calculation of σ has always been a challenge in the research on retrieval algorithm of ice particles (Lu et al. 2016). The main algorithms for computing the σ of non-spherical ice particles include T-matrix (Mackowski and Mishchenko 1996), discrete dipole approximation (DDA; Draine and Flatau 1994), and the Rayleigh–Gans approximation (RGA; Matrosov 1992; Westbrook et al. 2006). The T-matrix and DDA algorithm are too computationally expensive (Lu et al. 2016) to be suitable for massive calculations about the Doppler spectra, while the RGA algorithm computes much faster than the T-matrix and DDA and is overall more accurate than the classical Rayleigh and Mie solutions (Tyynelä et al. 2013).

By using the RGA algorithm, Hogan and Westbrook (2014) derived the equation for calculating the mean σ of aggregates at centimeter and millimeter wavelengths. Although the internal structure of an individual snowflake is random and unpredictable, Hogan and Westbrook (2014) found, from the simulations of the aggregation process, their structure is self-similar, which could be described by a power-law. They called this model the self-similar Rayleigh–Gans approximation (SSRGA). This algorithm is convenient and accurate. This paper applies the RGA algorithm to calculate the σ of plates and bullet rosettes, while the SSRGA algorithm is used for aggregates.

In the Rayleigh–Gans theory, the σ of an arbitrarily shaped particle illuminated by a plane wave propagating in the direction s is given by (e.g., van de Hulst 1957; Westbrook et al. 2006):

$$\sigma_b = \frac{9k^4 |K_i|^2}{4\pi} \left| \int_{-D/2}^{D/2} A(s) \exp(i2ks)\, ds \right|^2 \qquad (12)$$

where k is the wavenumber calculating by $1/\lambda$, and K_{i} is the Clausius-Mossotti factor of solid ice. The D and $A(s)$ here can be considered the same as D and A in 3.1. Note that $\exp(i2ks)$ can be replaced by $\cos(2ks) + i \sin(2ks)$.

Equation (12) is convenient for individual arbitrarily shaped particles for which $A(s)$ is known. For an ensemble of aggregates of the same size but with different internal structures, it is laborious to calculate the mean σ by Eq. (12). Hogan and Westbrook (2014) derives an equation for calculating the mean σ of an ensemble of aggregates with the same size and different shapes, which is shown as Eq. (13):

$$\begin{aligned}\langle \sigma_b \rangle = \frac{9\pi k^4 |K_i|^2 V^2}{16} \Bigg\{ &\cos^2(x) \left[\left(1+\frac{\kappa}{3}\right)\left(\frac{1}{2x+\pi} - \frac{1}{2x-\pi}\right) - \kappa \left(\frac{1}{2x+3\pi} - \frac{1}{2x-3\pi}\right) \right]^2 \\ &+ \beta \sum_{j=1}^{n} (2j)^{-\gamma} \sin^2(x) \left[\frac{1}{(2x+2\pi j)^2} + \frac{1}{(2x-2\pi j)^2} \right] \Bigg\} \end{aligned} \qquad (13)$$

where $x = kD$, $V = \int_{-D/2}^{D/2} A(s) ds$ is the volume of the particle, n is the times of Fourier transform when $A(s)$ is decomposed, j is the wavenumber index, $\gamma = 5/3$ is the power-law slope factor, κ is the kurtosis parameter, and β is the power-law prefactor. Regarding randomly oriented aggregates, $\kappa = 0.00$, $\beta = 0.45$ are for aggregates of bullet rosettes or columns, and $\kappa = -0.05$, $\beta = 0.51$ are for aggregates of plates (Hogan and Westbrook 2014). These types of aggregates are basically consistent with those described in Section 3.1. In this study, the mean σ calculated by Eq. (13) is regarded as the σ of a single aggregate particle with the size of D.

Equation (13) is applicable when the radar wavelength is longer than the size of individual monomers. Schmitt and Heymsfield (2014) reported ice monomer sizes up to 250 μm, which is much smaller than the wavelength of CVPR-FMCW (5.5 cm). Therefore, Eq. (13) is suitable for computing the σ of aggregates in this study.

4. Case Study

This section selects two typical events and periods to represent shallow and deep events, respectively. The retrieval results of N, IWC, and D_{m} during the typical periods are analyzed, and the differences between the inside and outside of the GCs and FSs are discussed. Subsequently, all the six events are analyzed statistically.

4.1. Deep event

The same period of 0020–0120 UTC during the 28 February 2015 event was selected to represent the deep events, as described in C20. Using the detection profiles obtained by the CVPR-FMCW, the corresponding spectral parameters were calculated and displayed as time–height sections (Fig. 2). Fig. 2a shows the detailed structure of GCs and FSs produced as a result of the high resolution of CVPR-FMCW. Relatively high upward and downward velocities were found near the echo top (Fig. 2b), where the spectral width (SW) was significantly larger than that of the underlying cloud (Fig. 2c). These characteristics were consistent with those of the GC region described in Rauber et al. (2017).

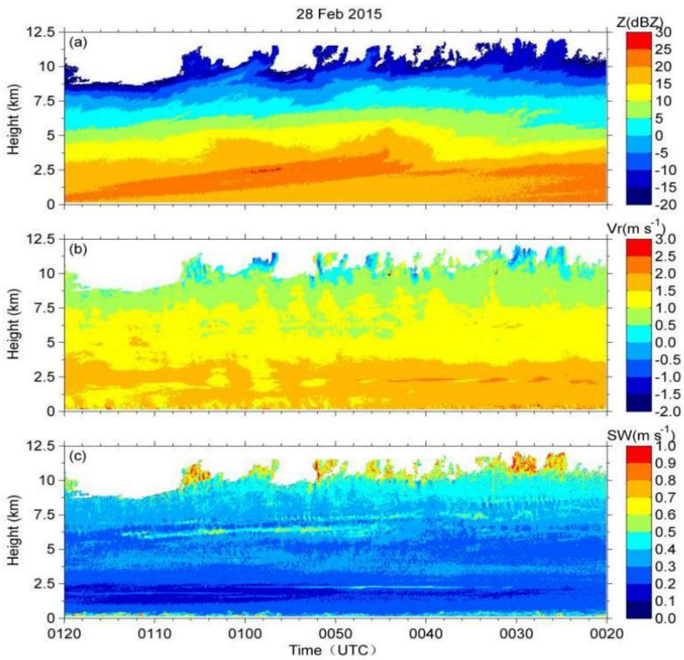

Fig. 2. The time–height plots from 0020 to 0120 UTC on 28 Feb 2015; (a) Z_e, (b) V_r (positive is downward), and (c) SW.

Below the GC region, the slanted streaks with large Z_e (in general, greater than 15 dBZ) were FSs, which embedded in the St region. Below about 7.5 km, the V_r was more uniform compared with the upper GC region, and the SW was narrower, mostly distributed in the range of 0–0.5 m s^{-1}, corresponding to the features of the St region. The obvious differences between the GC and St regions can be seen from the time–height plots of Z_e, V_r, and SW.

4.1.1 The differences in microphysical properties between GC and St regions

The method of dividing GC and St regions has been introduced in C20. For the deep events, this study still applies the vertical gradient of Z_e (dZ_e/dh) > 0.2 dB/30 m and the absolute value of vertical gradient of V_r ($|dV_r/dh|$) > 0.08 m s^{-1}/30 m as GC indicators to determine the height of the bottom of GCs. To calculate the depth of the GC region, the echo top height is also needed. Following the method of estimating the cloud top height described by Plummer et al. (2014), the thresholds of the Z_e and V_r variance were again adopted as −22dBZ and 0.8 m^2 s^{-2}, respectively (C20). Compared to the W-band radar used in Plummer et al. (2014), the C-band radar used in this article might not sensitive enough to capture small cloud ice particles, so we use "echo top" instead of "cloud top" in this study. As described in Section 3.1, we considered that the main particle types in the GC and St regions were different. For the deep events, the aggregates of plates, columns, and bullets were regarded as the dominant particle type in the St regions, and the GC regions were mainly composed of bullet rosettes.

Note that from the perspective of actual physical processes, although threshold values can determine the boundary of the two regions, the particle type does not suddenly change at the boundary. Therefore, the distance between the bottom of GCs and the echo top at each profile during the selected period was calculated, and the shortest distance was defined as the depth of the GC region. The region with distinct stratiform characteristics below 7.5 km was regarded as the St region. The part between the GC and St regions was regarded as the transition region, where the types of particles cannot be accurately judged; therefore, this study does not discuss the transition region.

The contoured frequency by altitude diagrams (CFADs) are useful to show the ensemble properties of variables at several heights over a time period (Yuter and

Houze 1995), which meet the requirement of statistical analysis of data at different heights and facilitate the contrast between deep and shallow events in this study. The CFADs of the retrieved N, D_m and IWC in GC region during the selected time period are shown in Figs. 3a, 3b, and 3c respectively. Since the calculated heights of the echo tops were not constant, the ordinates in Figs. 3a, 3b, and 3c were set as distance below the echo top instead of height above the ground. Most of N values (>80%) were less than 100 L^{-1} with a maximum of 305 L^{-1}. Near the echo top, the N values were mainly concentrated around 25 L^{-1}. As the height decreased, N tended to increase, and the proportion of values above 50 L^{-1} increased. The D_m values were mainly distributed between 200 and 400 μm with a maximum of 530 μm. With the decrease of height, D_m increased slowly, and the proportion of values above 300 μm increased. The IWC values were mainly distributed within 0.08 g m^{-3} with a maximum of 0.153 g m^{-3}. With the decrease in height, the IWC tended to increase, and the proportion of values above 0.03 g m^{-3} increased.

The changes in N, IWC, and D_m must be related to environmental T and humidity. The detected T and RH can be converted into actual vapor pressure (e) and supersaturation with respect to ice (S_i) by the WMO formulations, as shown in C20. The profiles of T, e, and S_i are shown in Figs. 3d, 3e, and 3f respectively. According to the average echo top height (calculated from echo top heights within the selected time period), the rough range of GC region was marked in Figs. 3d, 3e, and 3f. The corresponding T in the GC region ranged from −60°C to −50°C, and the e values were all below 10 hPa, indicating the little water vapor content. The S_i was greater than 30%

and reached a maximum of 40% near the echo top. The efficient ice formation exists below −38°C under water saturation (RH <100% in Fig. 1b), and the environment of low *T* and high S_i is conducive to the increase of ice activated fraction (Welti et al. 2014), leading to the large *N* values. Homogeneous ice nucleation may also occur in the GC region (Laksmono et al. 2015), which is conducive to the increase of *N*.

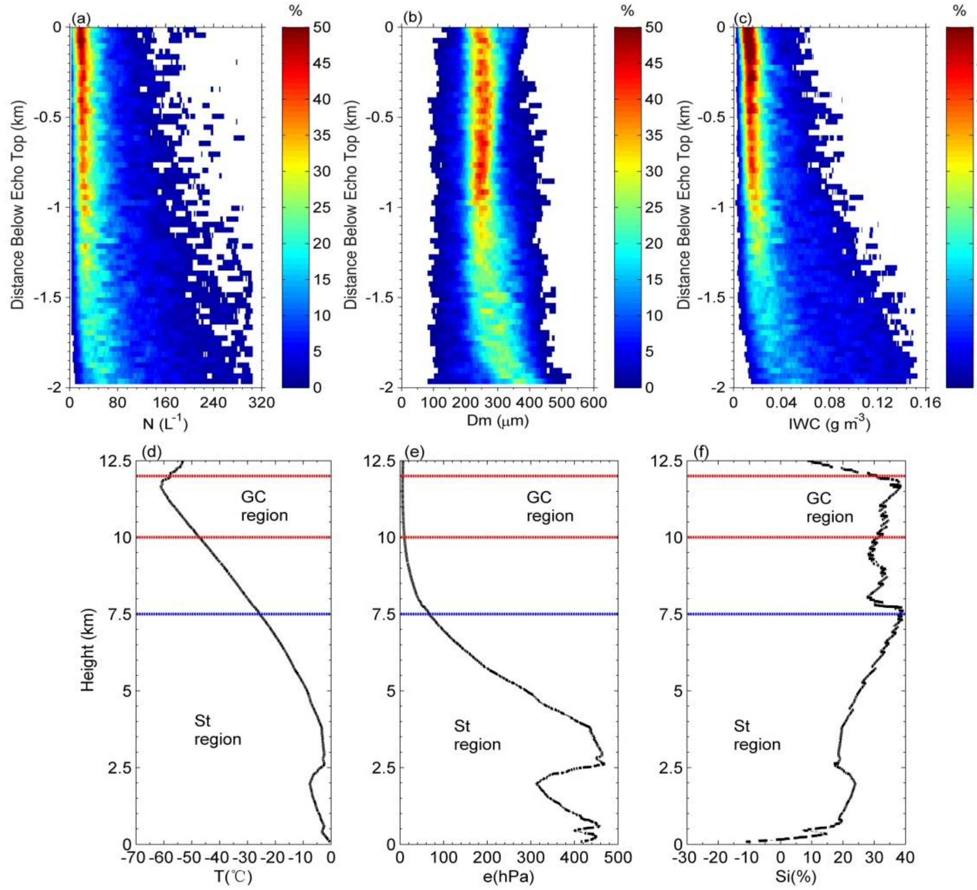

Fig. 3. The CFADs of (a) *N*, (b) D_m, and (c) IWC in the GC region during 0020 to 0120 UTC on 28 Feb 2015; and the profiles of (d) *T*, (e) *e* and (f) S_i at 0000 UTC on 28 Feb 2015 at Fuyang radiosonde station. The resolutions of CFADs are 20, 40 and 0.01 respectively for *N*, D_m, and IWC. In (d), (e), and (f), the rough range of GC region is between the two red lines, and the range of St region is below the blue line.

Due to the low T (< −40°C shown in Fig. 3d), it was impossible for riming to exist without supercooled water. The ice supersaturation in the GC region provided the conditions for continuous growth of ice particles. However, the water vapor content was low, resulting in the slow growth in particle size and the related D_m. At the low T, small particles can significantly contribute to IWC (Plummer et al. 2014). Therefore, IWC still increased obviously in the case of slow particle growth.

The CFADs of the retrieved N, D_m and IWC in St region are shown in Figs. 4a, 4b, and 4c respectively. Since the reliability of radar data near the ground is not high, the CFADs began with 500 m. The N values were mainly distributed within 80 L^{-1} with a maximum of 155 L^{-1}. The proportion for the range of 10–40 L^{-1} was the largest, reaching more than 30%. As height decreased, the D_m values initially increased and then decreased slightly with a maximum of 3600 μm. The IWC values were mainly distributed between 0.25 g m^{-3} and 1.25 g m^{-3}, with a maximum of 1.49 g m^{-3}. With the decrease in height, the IWC values also showed a trend of increasing first and then decreasing, and the values increased slightly below 1 km.

As shown in Fig. 4, the N values in the St region were smaller than those in the GC region. In the St region, the T was basically higher than −25°C (Fig. 3d). The aggregation and the negative effect of the warmer T (compared to the T in GC region) on ice nucleation might be the reasons for the decrease in the N values. The N values increased evidently near 4 km, 2.5 km, and 1 km. Combined with the T profile of St region (Fig. 3d), it was found that the corresponding T of the above three heights were about −5°C, which was exactly the T with the greatest production rate of secondary ice particles in the Hallett–Mossop process (Mossop 1976). The production of secondary ice particles increased *N* and IWC, which was consistent with the phenomenon described in Keppas et al. (2018). The secondary particles generated by the Hallett–Mossop process are usually columnar (Heymsfield and Willis 2014), with an average diameter of 120 μm (Zawadzki et al. 2001). The bimodal Doppler spectra also indicated the possible existence of small secondary ice crystals as described in the relevant studies (e.g., Zawadzki et al. 2001), and the bimodal spectra near 4 km are shown in Fig. 4d as an example. Similar to C20, to clearly show the bimodal phenomenon, the ordinate in Fig. 4d is represented by normalized power and all Doppler spectra are smoothed using a three-point boxcar averaging window. The heights of the spectra are also marked in Fig. 4d.

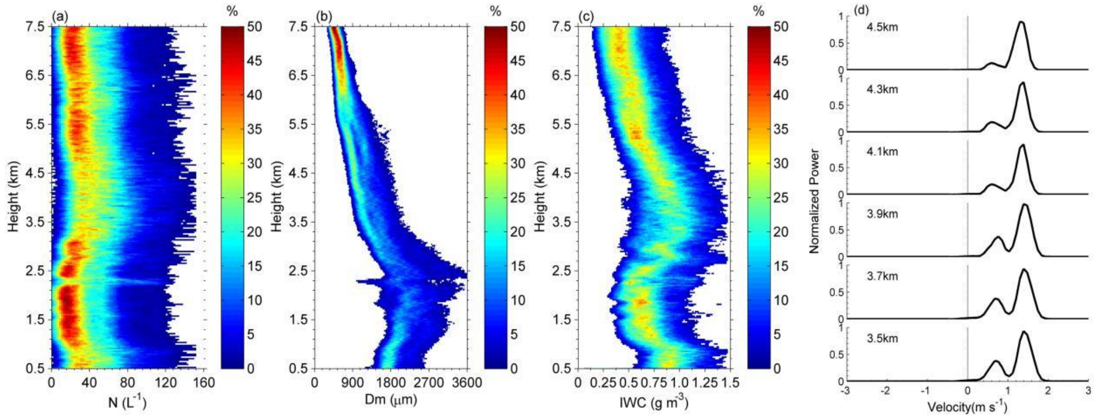

Fig. 4. The CFADs of (a) *N*, (b) D_m, and (c) IWC in the St region during 0020 to 0120 UTC on 28 Feb 2015; and (d) is the diagram of normalized bimodal spectra between 3.5 and 4.5 km. The resolutions of CFADs are 20, 100, and 0.1 respectively for *N*, D_m, and IWC.

Although we believe that the existence of the bimodal spectra is related to the

Hallett–Mossop process, the influence of wind shear cannot be ignored. The wind shear may contribute to bimodal spectra because of particle size sorting, time evolution of fall streaks, and inhomogeneity of cloud systems (e.g., Kumjian and Ryzhkov 2012; Dawson et al. 2015).

Note that this paper assumed that the St regions were mainly composed of aggregates, and only considered this particle type when retrieving the microphysical parameters. Therefore, there might be some deviations in the description of small ice particles, but the increase in the number concentration of small particles can still be reflected by the changes in N.

The D_m represented the median volume diameter of particles within each range gate, so the response to the secondary ice particles was not obvious. Between 2.5 and 7.5 km, the D_m increased with the decrease in height. According to Figs. 3d, 3e, and 3f, the ice particles can grow continuously in this range because of ice supersaturation, and e increased with the decrease in height, which was more conducive to the deposition growth. Moreover, the T in this range was between −25°C and −2°C, including the T conducive to aggregation (−20 to −10°C according to Connolly et al. 2012). We speculated that the decrease in D_m below 2.5 km might be caused by the reduction in e and S_i.

4.1.2 The differences between the inside and outside of GCs and FSs

According to the differences in Z_e between the surrounding regions and the inside of GCs and FSs (Fig. 2a), the N, D_m and IWC inside and outside GCs and FSs were presumed to be different. Similar to C20, the threshold of 4 dB relative maxima in the Z_e time series measurements was used to identify the inside of GCs, as presented by Plummer et al. (2014). Due to the larger Z_e values inside FSs compared to outside, measurements above the 60th-percentile Z_e values in moving time windows were classified as FSs (Plummer et al. 2015) by using the 45 s window (C20). Figure 5 shows the statistical distributions of microphysical parameters inside and outside GCs and FSs at four equally-spaced heights with boxplots. The boxplots include the median and 5th, 25th, 75th, and 95th percentiles of N, D_m, and IWC during the selected period. The plots in blue represent the inside of GCs or FSs, and the plots in red represent the outside.

The boxplots of N, D_m, and IWC inside and outside GCs at 0.5, 1, 1.5, and 2 km below the echo top are exhibited in Figs. 5a, 5b, and 5c, and the corresponding T of the four heights are marked in Fig. 5a. At all heights, the median and statistical percentiles of N, D_m, and IWC were higher inside GCs compared to outside. The variation trends of these three parameters with height were similar to those reflected by the CFADs and the variation trends of these parameters inside and outside GCs were basically the same. With the decrease in height and the increase in T, the N values inside and outside GCs showed an increasing trend, so did the IWC values. As height decreased, the changes of D_m inside and outside GCs were not apparent, but the 95th percentile of D_m inside GC increased, which was caused by the slow growth mentioned in Section 4.1.1.

With the decrease in height, the increments in median and statistical percentiles of

N, D_m, and IWC inside GCs were greater than those outside GCs. The N, D_m, and IWC values inside GCs were larger and grew more rapidly compared to outside, which might be associated with the differences in dynamical properties. The GC locations were usually accompanied by upward air motion, whereas downward air motions often appeared between GCs (C20). The upward air motion brings more water vapor for ice growth and enhances the activated rate of ice nuclei (e.g., Crosier et al. 2014), resulting in larger values of N, D_m, and IWC inside GCs.

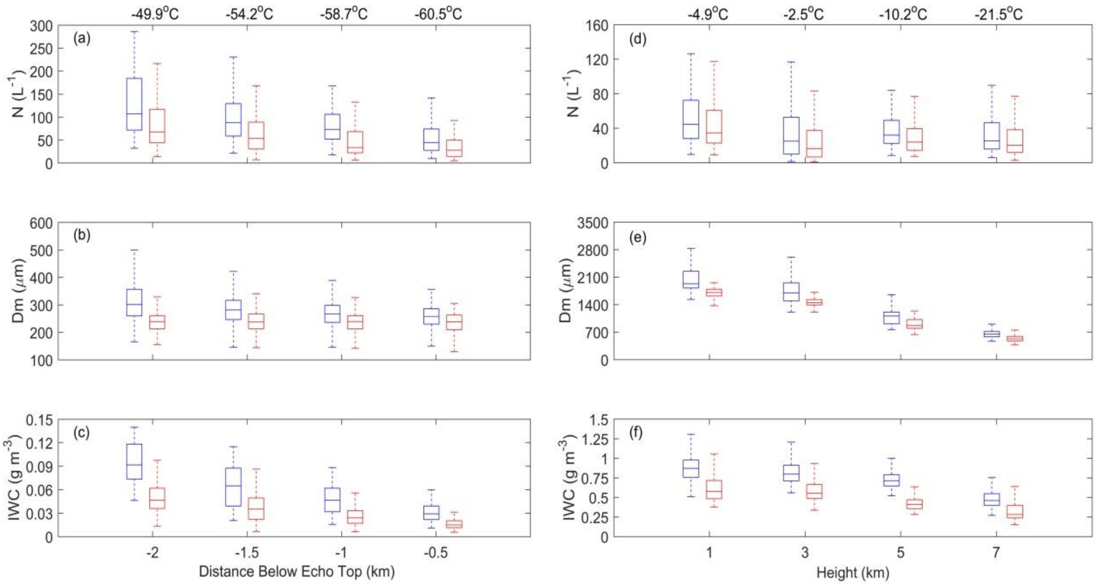

Fig. 5. The boxplots of (a) N, (b) D_m and (c) IWC inside and outside GCs and (d) N, (e) D_m and (f) IWC inside and outside FSs during 0020 to 0120 UTC on 28 Feb 2015. The plots in blue represent the inside of GCs or FSs, and the plots in red represent the outside.

The boxplots of N, D_m, and IWC inside and outside FSs at 1, 3, 5, and 7 km are exhibited in Figs. 5d, 5e, and 5f, and the corresponding T of the four heights are marked in Fig. 5d. Similar to the GC region, the median and statistical percentiles of

N, D_m, and IWC were higher inside FSs compared to outside at all heights, and the variation trends of these values inside and outside FSs were basically the same. However, both D_m and IWC values inside and outside FSs were higher than those in the GC region, while the N values inside and outside FSs were lower, implying the existence of aggregation and deposition growth inside and outside FSs. The variation trends of the three parameters with height were also similar to those reflected by the CFADs. From 7 to 5 km, the slightly reduced N might be due to the suitable temperature (between −20 and −10°C) for aggregation (Connolly et al. 2012). The large N values at 3 km and 1 km might be associated with multiplication of ice particles, as mentioned in Section 4.1.1. From 7 to 3 km, the median and statistical percentiles of D_m and IWC inside and outside FSs showed an obvious increasing trend with the decrease in height, while those at 1 km were slightly larger compared to 3 km, which is probably due to the slow deposition growth of ice particles related to the reduction in e and S_i below 2.5 km.

4.2 Shallow event

The same period of 1230–1330 UTC during the 20 January 2016 event was selected to represent the shallow events, as described in C20. The Z_e, V_r, and SW are exhibited by the time–height contours in Fig. 6, indicating that the main distribution characteristics of spectral parameters were similar to those in the deep event. Figure 6a shows the detailed structure of the GCs and FSs, and upward and downward air motions coexisted near the echo top (Fig. 6b), where the SW was apparently larger than that of the underlying cloud (Fig. 6c). Below about 3.5 km, the V_r was more uniform and the SW was narrower (within 0.4 m s^{-1}) compared with the upper region, corresponding to the features of the St region. The obvious differences between the GC and St regions can also be seen from the time–height plots of Z_e, V_r, and SW.

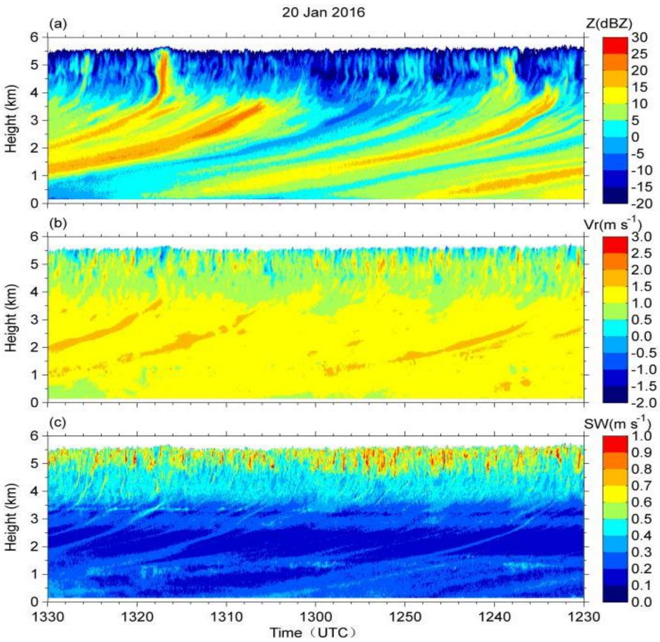

Fig. 6. The time–height plots from 1230 to 1330 UTC on 20 Jan 2016; (a) Z_e, (b) V_r (positive is downward), and (c) SW.

4.2.1 The differences in microphysical properties between GC and St regions

For the shallow events, $dZ_e/dh > 0.6$ dB/30 m and $|dV_r/dh| > 0.08$ m s^{-1}/30 m were used as GC indicators to determine the height of the bottom of GC (C20). Following the method of estimating the echo top altitude described by Plummer et al. (2014), the thresholds of Z_e and V_r variance were again adopted as −28 dBZ and 0.8 m^2 s^{-2}, respectively (C20). As in Section 4.1, the height of the echo top was determined and the depth of the GC region (0.9 km) was calculated. The region with distinct stratiform characteristics below 3.5 km was regarded as the St region. For the shallow events, the aggregates of plates were regarded as the dominant particle type in the St regions and the GC regions were mainly composed of hexagonal plates. The part between the GC and St regions was regarded as the transition region, where the types of particles cannot be accurately judged; therefore, this study does not discuss the transition region.

The CFADs of the retrieved N, D_m, and IWC in GC region are shown in Figs. 7a, 7b, and 7c respectively. The N values were mainly distributed within 80 L^{-1} with a maximum of 198 L^{-1}. The proportion for the range of 0–20 L^{-1} was the largest, reaching more than 20% at all heights. The D_m values were mainly distributed between 200 and 600 μm with a maximum of 800 μm. With the decrease in height, D_m showed an increasing trend, and the proportion of values above 400 μm increased. The IWC values were mainly distributed within 0.08 g m^{-3} with a maximum of 0.197 g m^{-3}. Compared with the deep event, the range of N was smaller, and the proportion of large values was less. The maximum values of D_m and IWC were larger than those in the deep event, and the distribution ranges of D_m and IWC were wider. As height decreased, the D_m showed a more obvious increase.

Similar to Figs. 3d–3f, the GC and St regions were also marked in Figs. 7d–7f. According to the profiles of T, e, and S_i in Fig. 7, the corresponding T in the GC region ranged from −21°C to −15°C, and e values were between 100 and 200 hPa. The S_i was greater than 30% and reached a maximum of 40% near the echo top. Compared with the GC region of the deep event, S_i was similar, but the T increased, resulting in the decrease of ice activated fraction and reduction in the concentration of ice nuclei (Welti et al. 2014), which caused the smaller N values. The environment of ice supersaturation was conducive to the deposition growth of ice particles, and the water vapor was more abundant, enabling the ice particles to grow further. At the same time, because of the higher temperatures in the GC region, supercooled water might exist (Plummer et al. 2014), causing the riming growth. Therefore, in the GC region of the shallow event, D_m increased rapidly within the range of 0.9 km.

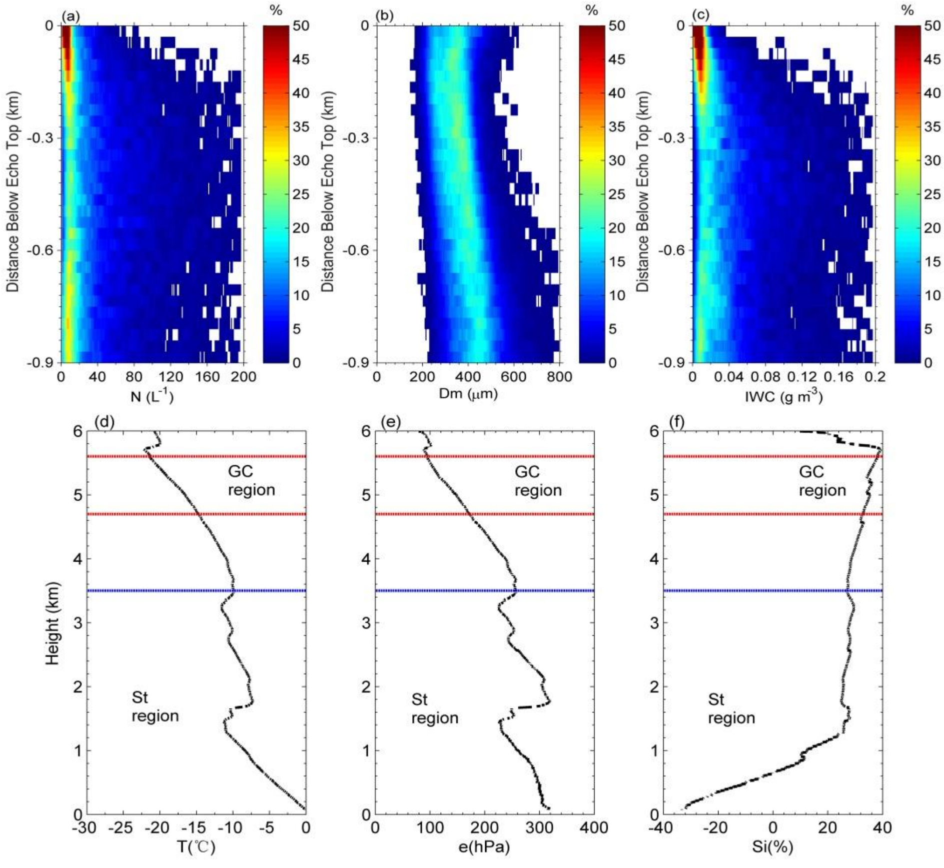

Fig. 7. The CFADs of (a) N, (b) D_m, and (c) IWC in the GC region during 1230 to 1330 UTC on 20 Jan 2016; and the profiles of (d) T, (e) e and (f) S_i at 1200 UTC on 20 Jan 2016 at Fuyang radiosonde station. The resolutions of CFADs are 10, 40 and 0.01 respectively for N, D_m, and IWC. In (d), (e), and (f), the rough range of GC region is between the two red lines, and the range of St region is below the blue line.

Between 0.6 and 0.9 km below the echo top, the proportion for small N values (within 20 L^{-1}) increased compared with the range between 0.3 and 0.6 km below the echo top, which might be caused by aggregation. Although hexagonal plates were considered to be predominant in the GC region, aggregation might exist at the suitable T. The T within this area was distributed around −15°C, corresponding to the higher aggregation efficiency compared to the area above (Connolly et al. 2012), which led to a decrease in N. The decrease of N in this area also affected the IWC values slightly. Although from the perspective of microphysics, the aggregation has no influence on IWC, the calculating equation of IWC (Eq. 3) determines that the IWC is proportional to N, and the change of N has a more direct impact on IWC compared to D_m. The nature of Eq. 3 causes the limitation of retrieving IWC. Since in addition to N, the values of IWC are affected by m, the limitation has little impact on the retrieval of IWC values, but only makes the variation trends of IWC presented in the CFADs more similar to those of N compared to D_m.

The CFADs of the retrieved N, D_m, and IWC in St region are shown in Fig. 8. The CFADs also began with 500 m. Most of N values (>80%) were less than 50 L^{-1} with a maximum of 118 L^{-1}. The D_m values were mainly distributed between 600 and 2000 μm with a maximum of 3600 μm. As height decreased, the maximum D_m values initially increased and then decreased slightly. The IWC values were mainly distributed within 0.75 g m^{-3} with a maximum of 1.48 g m^{-3}. Compared with the St region of the deep event, the maximum value of N decreased, while the maximum values of D_m and IWC remained almost unchanged. The large values of N and IWC (more than 50 L^{-1} and 0.75 g m^{-3}, respectively) accounted for a lower proportion during the shallow event.

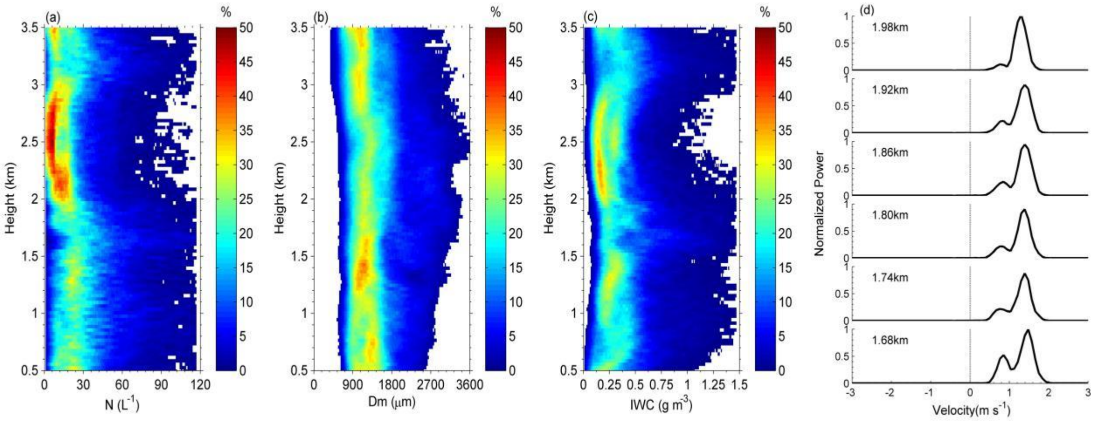

Fig. 8. The CFADs of (a) N, (b) D_m, and (c) IWC in the St region during 1230 to 1330 UTC on 20 Jan 2016; and (d) is the diagram of normalized bimodal spectra between 1.68 and 1.98 km. The resolutions of CFADs are 10, 300, and 0.1 respectively for N, D_m, and IWC.

The N values increased around 1.7 km and 0.8 km. According to the T profile of St region in Fig. 7d, the corresponding T near the above two heights were between −3°C and −8°C, which might be associated with Hallett–Mossop process (Mossop 1976). The production of secondary ice particles also increased the IWC at the same heights. The bimodal Doppler spectra near 1.7 km shown in Fig. 8d as an example, also indicated the possible existence of small secondary ice crystals, but note that the influence of wind shear cannot be ruled out. The heights of the spectra are marked in Fig. 8d. Between 1.7 and 3.5 km, the D_m increased with the decrease in height. The environment of ice supersaturation and increasing e (Figs. 7e and 7f) was conducive to the deposition growth of ice particles, and riming along with aggregation might also exist. The aggregation efficiency was relatively high between 2.5 and 3.5 km because of the appropriate T for aggregation (between −12°C and −10°C), leading to the reduction in N and IWC. The decrease in the maximum D_m values below 1.7 km might be caused by the reduction in e and S_i, as shown in Figs. 7e and 7f.

4.2.2 The differences between the inside and outside of GCs and FSs

For the shallow event, we still used the method described in Section 4.1.2 to distinguish the inside and outside of the GCs and FSs and discussed whether there were differences in microphysical properties between them. Figure 9 shows the statistical distributions of microphysical parameters inside and outside GCs and FSs at four equally-spaced heights by the boxplots. The boxplots include the median and 5th, 25th, 75th, and 95th percentiles of N, D_m, and IWC during the selected period.

The boxplots of N, D_m and IWC inside and outside GCs at 0.2, 0.4, 0.6, and 0.8 km below the echo top are exhibited in Figs. 9a, 9b, and 9c respectively, and the corresponding T of the four heights are marked in Fig. 9a. At all heights, the median and statistical percentiles of N, D_m, and IWC were higher inside GCs compared to outside. The variation trends of these three parameters with height were similar to those reflected by the CFADs. Between 0.2 and 0.6 km below the echo top, with the decrease in height and the increase in T, the N, D_m, and IWC values inside and outside the GCs showed an increasing trend, while under 0.6 km below the echo top, N and IWC values inside and outside the GCs decreased. With the decrease in height, the increments in the median and statistical percentiles of N, D_m, and IWC inside GCs were greater than those outside GCs. The dynamical properties were similar to those in the GC region of the deep event (C20). The N, D_m, and IWC values inside GCs were larger and grew more rapidly compared to outside, which might be related to the upward air motions inside GCs.

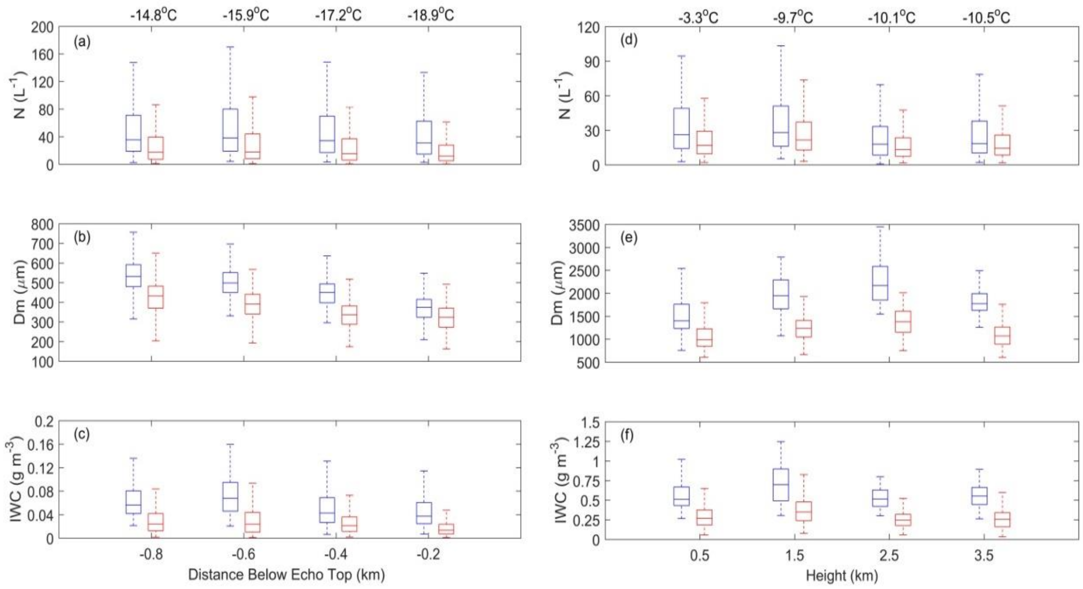

Fig. 9. The boxplots of (a) N, (b) D_m and (c) IWC inside and outside GCs and (d) N, (e) D_m and (f) IWC inside and outside FSs during 1230 to 1330 UTC on 20 Jan 2016. The plots in blue represent the inside of GCs or FSs, and the plots in red represent the outside.

The boxplots of N, D_m, and IWC inside and outside FSs at 0.5, 1.5, 2.5, and 3.5 km are exhibited in Figs. 9d, 9e, and 9f, and the corresponding T of the four heights are marked in Fig. 9d. Similar to the GC region, the median and statistical percentiles of N, D_m, and IWC were higher inside FSs compared to outside at all heights. Both D_m and IWC values inside and outside FSs were larger than those in the GC region, while the N values inside and outside FSs were lower, implying the existence of aggregation and deposition growth inside and outside FSs. Aggregation and multiplication of ice particles, as mentioned in Section 4.2.1, affected the changes of N, D_m, and IWC inside and outside FSs at the four heights. From 1.5 to 0.5 km, the median and statistical percentiles of D_m and IWC inside and outside FSs showed a decreasing trend, possibly due to the effect of decreasing S_i. The negative values of S_i below about 0.7 km led to the sublimation of ice particles, causing the reduction in particle size and mass.

4.3 Statistical analysis of six snow events

Sections 4.1 and 4.2 only discussed the typical periods of deep and shallow events in detail. In this section, all six events were statistically analyzed to discuss the similarities and differences in the microphysical parameters of two regions in the two event types and to compare the differences between the inside and outside of the GCs and FSs.

4.3.1. Statistical analysis of microphysical parameters in GC and St regions

Table 3 summarizes the ranges of the retrieved N, D_m, and IWC in the GC and St regions during the six events. In the GC regions, compared with the deep events, the N values in the shallow events were smaller, while the values of D_m and IWC were larger. For the shallow events, the average depth of the GC regions was 1.2 km. The N, D_m, and IWC mainly showed an increasing trend with the reduction in height. The average increment in N reached 215 L^{-1}, with a growth rate of 178 L^{-1} km^{-1}. The average increment in D_m reached 757 μm, and that of IWC reached 0.24 g m^{-3}, with growth rates of 631 μm km^{-1} and 0.2 g m^{-3} km^{-1}, respectively. For the deep events, the average depth of the GC regions was 1.9 km. The average increments in N, D_m, and IWC were 370 L^{-1}, 547 μm, and 0.17 g m^{-3}, with growth rates of 195 L^{-1} km^{-1}, 288 μm km^{-1}, and 0.09 g m^{-3} km^{-1}, respectively. These statistics indicate that in the GC regions of shallow events, N increased more slowly while D_m and IWC increased more rapidly compared to the deep events. The T and RH_i ranges of the GC regions during the events of the same type were similar (Table 3 in C20). Therefore, these phenomena can be explained from the perspective of environmental T and humidity as described in Section 4.2.1.

In the St regions, the distribution ranges of N in the shallow events were narrower than those in the deep events. Compared with the GC regions, N decreased while D_m and IWC increased during the six events, implying the existence of aggregation and deposition growth. For the shallow events, the increments in the maximum values of D_m and IWC between the St and GC regions are defined as ΔD_m and ΔIWC within the St regions, with the average values of 3116 μm and 1.71 g m^{-3} respectively. The maximum values of D_m and IWC in the St regions are the same as those in the entire clouds, named D_{max} and IWC_{max} respectively. The ratio of ΔD_m within the St region to the D_{max} is defined as the contribution of the St region to the growth of the D_m. The contribution to the growth of IWC was calculated in the same way. The average contributions of St regions to the growth of D_m and IWC were 80% and 88%, respectively. For the deep events, the average values of ΔD_m and ΔIWC within the St regions were 3403 μm and 1.85 g m^{-3} respectively, and the average contributions of St regions to the growth of D_m and IWC were 86% and 91%, respectively. The results indicated that the growth of particle size and mass mainly occurred in the St regions, which corresponded well with the previous studies (e.g., Matejka et al. 1980; Houze et al. 1981; Plummer et al. 2015).

Table 3: The ranges of retrieved N, D_m and IWC in GC and St regions during the shallow and deep snow events.

		GC region			St region		
Event type	Date	N (L^{-1})	D_m (μm)	IWC (g m^{-3})	N (L^{-1})	D_m (μm)	IWC (g m^{-3})
Shallow	27 Jan 2015	1–211	80–806	0–0.23	1–123	457–3893	0.10–1.84
	28 Jan 2015	1–229	61–851	0–0.27	1–133	403–4128	0.14–2.16
	29 Jan 2015	1–215	65–835	0–0.25	1–119	426–4066	0.07–2.03
	20 Jan 2016	1–207	72–812	0–0.22	1–127	470–3680	0.02–1.79
Deep	28 Feb 2015	1–363	50–583	0–0.16	1–189	312–3975	0.11–1.98
	24 Nov 2015	1–378	46–607	0–0.17	1–196	336–4021	0.09–2.05

4.3.2. Statistical analysis of N, D_m, and IWC inside and outside GCs and FSs

The ranges of median N, D_m, and IWC inside and outside GCs during the six events are summarized in Table 4. Compared with the deep events, the medians of N inside and outside GCs were smaller in the shallow events, and the medians of D_m and IWC were larger. For all events, the medians of N, D_m, and IWC inside GCs were greater than those outside GCs. Since the distribution ranges of median N, D_m and IWC are different for each event, the common ranges for all events of the same type are defined as the main distribution ranges to further study.

Table 4: The ranges of median N, D_m and IWC inside and outside GCs during the shallow and deep snow events.

		Med. N (L^{-1})		Med. D_m (μm)		Med. IWC ($g\ m^{-3}$)	
Event type	Date	Inside GC	Outside GC	Inside GC	Outside GC	Inside GC	Outside GC
Shallow	27 Jan 2015	30–42	12–22	336–564	291–458	0.02–0.07	0.01–0.03
	28 Jan 2015	25–51	9–29	311–586	284–473	0.03–0.10	0.01–0.05
	29 Jan 2015	21–47	8–28	323–572	277–465	0.02–0.09	0.01–0.04
	20 Jan 2016	27–43	10–24	340–553	298–451	0.03–0.07	0.01–0.03
Deep	28 Feb 2015	36–131	17–72	245–310	204–243	0.02–0.09	0.01–0.05
	24 Nov 2015	31–138	20–69	232–303	189–240	0.03–0.08	0.01–0.04

For the shallow events, the main distribution ranges of median N, D_m, and IWC were 30–42 L^{-1}, 340–553 μm, and 0.03–0.07 $g\ m^{-3}$ inside GCs, and 12–22 L^{-1}, 298–451 μm, and 0.01–0.03 $g\ m^{-3}$ outside GCs, respectively. The average ratios of the median N, D_m, and IWC inside GCs to those outside GCs are 2, 1.3, and 2.5 respectively. For the deep events, the main distribution ranges of median N, D_m, and

IWC were 36–131 L^{-1}, 245–303 μm, and 0.03–0.08 g m^{-3} inside GCs, and 20–69 L^{-1}, 204–240 μm, and 0.01–0.04 g m^{-3} outside GCs, respectively. The average ratios of the median N, D_m, and IWC inside GCs to those outside GCs are 1.7, 1.2, and 2.3 respectively. The differences in N, D_m, and IWC between the inside and outside of GCs might be due to the influence of dynamical properties, as described in Section 4.1.2.

The ranges of median N, D_m, and IWC inside and outside FSs during the six events are summarized in Table 5. Compared with the GC regions, the medians of N inside and outside FSs were smaller, and the medians of D_m and IWC were larger. For all events, the medians of N, D_m, and IWC inside FSs were greater than those outside FSs. For the shallow events, the main distribution ranges of median N, D_m, and IWC were 15–31 L^{-1}, 1195–2183 μm, and 0.47–0.82 g m^{-3} inside FSs, and 7–17 L^{-1}, 786–1456 μm, and 0.21–0.41 g m^{-3} outside FSs, respectively. The average ratios of the median N, D_m, and IWC inside FSs to those outside FSs are 2, 1.4, and 2.5 respectively, which were basically the same as the average ratios for the GC regions of shallow events. For the deep events, the main distribution ranges of median N, D_m, and IWC were 23–61 L^{-1}, 853–2096 μm, and 0.41–0.87 g m^{-3} inside FSs, and 12–34 L^{-1}, 552–1625 μm, and 0.19–0.53 g m^{-3} outside FSs, respectively. The average ratios of the median N, D_m, and IWC inside FSs to those outside FSs are 1.7, 1.3, and 2.3 respectively, which were basically the same as the average ratios for the GC regions of deep events.

There was no apparent difference in W_a inside and outside the FSs (C20), resulting in the similar conditions for the growth and nucleation of ice particles inside and outside FSs. Moreover, the FSs were formed by falling snow particles originated from GCs, and the differences in N, D_m, and IWC between the inside and outside of GCs and FSs were almost the same, implying the importance of GCs to the enhanced ice growth subsequently found in FSs, which corresponded well with previous studies (Plummer et al. 2014; Plummer et al. 2015).

Table 5: The ranges of median N, D_m and IWC inside and outside FSs during the shallow and deep snow events.

		Med. N (L^{-1})		Med. D_m (μm)		Med. IWC (g m^{-3})	
Event type	Date	Inside FS	Outside FS	Inside FS	Outside FS	Inside FS	Outside FS
Shallow	27 Jan 2015	15–31	7–17	1132–2195	772–1475	0.45–0.82	0.19–0.41
	28 Jan 2015	12–39	5–23	1059–2436	721–1529	0.39–0.91	0.17–0.47
	29 Jan 2015	13–36	6–20	1087–2304	735–1518	0.43–0.90	0.20–0.45
	20 Jan 2016	15–35	7–20	1195–2183	786–1456	0.47–0.85	0.21–0.42
Deep	28 Feb 2015	23–61	12–35	704–2096	495–1738	0.38–0.91	0.19–0.60
	24 Nov 2015	21–62	10–34	853–2130	552–1625	0.41–0.87	0.18–0.53

4.4. Z_e–IWC relationship and error discussion

4.4.1. Z_e–IWC relationship

After obtaining the retrieved IWC and the Z_e measured by CVPR-FMCW, we attempt to establish Z_e–IWC relationship for snow clouds in the midlatitudes of China.

Many studies have reported Z_e–IWC relationships for different radar wavelengths in different regions (e.g., Hogan et al. 2006; Protat et al. 2007; Heymsfield et al. 2005). From all of these studies, the variability of Z_e–IWC relationships in space and time can be found.

The Z_e–IWC power-law relationship with the generic form of IWC = aZ_e^b can be established by fitting. During the winter of 2015–2016 with the cumulative snowfall duration of 37 h and 39 min, the 1988571 effective data points in 26540 radar detection profiles were fitted as shown in Fig. 10. The obtained Z_e–IWC relationship is shown as Eq. (14), represented by the black solid line in Fig. 10:

$$IWC = 0.18Z_e^{0.38} \quad (14)$$

where the unit of IWC is g m^{-3}, the unit of Z_e is mm^6 m^{-3}. The quality of fit for Eq. (14) was indicated by an R^2 value of 0.9063, with a root mean square error (RMSE) of 0.087, which represented a good fit.

In Fig. 10, Eq. (14) is also compared with Z_e–IWC relationship in other studies. Due to the weak attenuation of electromagnetic wave caused by snow particles, the detection difference between X-band and C-band radars is ignorable. Therefore, the relationships established based on the measurements of X-band radars were chosen for reference. Heymsfield et al. (2016) directly related the IWC measured in situ by a counterflow virtual impactor probe to the Z_e measured by an airborne X-band radar, which obtained the relationship given by the following Eq.:

$$IWC = 0.159Z_e^{0.422} \quad (15)$$

Heymsfield et al. (2005) developed the piecewise Z_e–IWC relationships for different ranges of reflectivity detected by an X-band radar:

$$IWC = \begin{cases} 0.143 Z_e^{0.39}, 0.0054 < Z_e < 8.09 \\ 0.179 Z_e^{0.29}, Z_e > 8.09 \end{cases} \quad (16)$$

Heymsfield et al. (2013) calculated IWC by the measured ice particle size distributions and established a Z_e–IWC relationship:

$$IWC = 0.134 Z_e^{0.427} \quad (17)$$

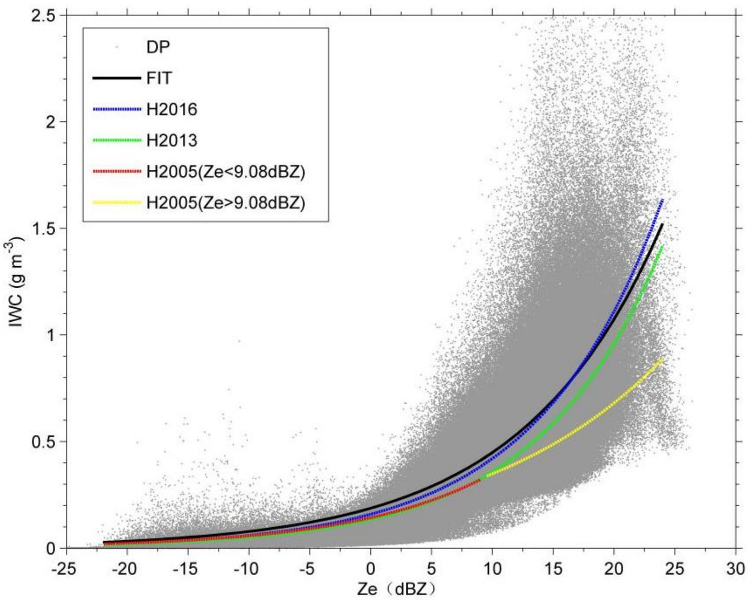

Fig. 10. Fitting curve of the Z_e–IWC relationship and comparison results with the relationships in Heymsfield et al. 2016, Heymsfield et al. 2013 and Heymsfield et al. 2005, abbreviated as H2016, H2013 and H2005 respectively. DP represents the data points, and FIT represents the fitting curve.

It can be seen from Fig. 10 that the fitted curve is very close to the curve obtained by Eq. (15). For a given Z_e, Eq. (17) yields lower IWC value compared to Eq. (14), with the maximum deviation of about 0.1 g m^{-3}. When $0.0054 < Z_e < 8.09$ mm^6 m^{-3} (between −22.68 and 9.08 dBZ), the IWC calculated by Eq. (16) is slightly lower than that calculated by Eq. (14) for a given Z_e. When $Z_e > 8.09\ \mathrm{mm}^6\ \mathrm{m}^{-3}$ (larger than 9.08 dBZ), the deviations between IWC values calculated by Eq. (16) and the other equations rise with the increase of Z_e. Heymsfield et al. (2016) inferred that the deviations may be caused by the different sampling case.

4.4.2 Error discussion

It is assumed that the CVPR-FMCW used in this study has almost no attenuation in snowfall detection, and its power spectral density distribution can accurately reflect the size distribution of snow particles. However, the retrieval errors of microphysical parameters are inevitable. The errors are caused by: 1) the hypothesis of particle types; 2) calculation of σ; 3) V_t-related errors.

We supposed that the GC regions of shallow events were dominated by hexagonal plates, while the GC regions of deep events were mainly composed of bullet rosettes, and the St regions in the two types of snow events were mainly composed of aggregates. We also assumed that there was only one particle type in a single radar sampling volume. The particle types affect the selection of m–D and A–D relationships, thus affecting the calculated m and A. Then the m and A affect the calculation of IWC, σ and V_t–D relationship. The particle types adopted in this study have been tested in C20, which is more in line with the given snow events, so that the error caused by hypothesis of particle types can be reduced here.

In the case of the present radar band and particle types, the RGA underestimates the σ of particles compared to the more accurate DDA algorithm (Tyynelä et al. 2013).

SSRGA is a method developed on the basis of RGA algorithm to calculate the σ of aggregates, with similar accuracy to RGA (Hogan and Westbrook 2014). According to Eqs. (2) and (3), it can be inferred that underestimating σ leads to the overestimation of N and IWC, which basically has no influence on D_m.

The V_t-related errors originate from the process of obtaining V_t from the V_r observed by CVPR-FMCW and the V_t–D relationships. The retrieved V_z values in St regions were underestimated by 0.16 m s^{-1} at most (C20), which was about 10% of the V_z values. The V_z was regarded as V_t leading to the slightly underestimation of V_t. The underestimation of V_t affects D by V_t–D relationships, then affecting m, A and σ. Since Re in the V_t–D relationship is associated with m and A, the errors of calculating D from V_t are different for different particles.

5. Conclusions

This study used the CVPR-FMCW with high resolution to obtain the continuous observation data of six snow events during the winter of 2015–2016 in the midlatitudes of China. The GCs described in previous studies were found near the echo tops in every event. Among the six events, four events were shallow, with the echo top mainly below 8 km. The other two events were deep, with the echo top mostly above 10 km. The N, D_m, and IWC were retrieved by radar Doppler spectra based on the W_a calculated in C20 to analyze the evolution of the microphysical properties in snow clouds. Finally, the first Z_e–IWC relationship suitable for snow clouds in the midlatitudes of China was established. The main conclusions are as follow:

(1) Similar to C20, the clouds were divided into upper GC and lower St regions. For the GC regions, hexagonal plates were regarded as the dominant particle type in the shallow events, with bullet rosettes for the deep events. For the St regions, the aggregates of plates were regarded as the main particle type in the shallow events, with the aggregates of plates, columns, and bullets for the deep events.

(2) In the GC regions, N values in the shallow events were smaller but D_m and IWC values were larger than those in the deep events. The N, D_m, and IWC mainly showed an increasing trend with the reduction in height. The average growth rates of N, D_m, and IWC were 178 L^{-1} km^{-1}, 631 μm km^{-1}, and 0.2 g m^{-3} km^{-1} respectively for shallow events, with 195 L^{-1} km^{-1}, 288 μm km^{-1}, and 0.09 g m^{-3} km^{-1} respectively for deep events. These statistics indicated that compared to the deep events, N increased more slowly, while D_m and IWC increased more rapidly in the shallow events. During the shallow events, the higher T compared to the deep events caused the decrease in ice activated fraction and reduction in the concentration of ice nuclei, which were adverse to the increase in N, while the more abundant water vapor and possibly existing supercooled water were conducive to the increase in D_m and IWC.

(3) In the St regions, the distribution ranges of N in the shallow events were narrower than those in the deep events. Compared with the GC regions, N decreased while D_m and IWC increased during the six events, implying the

existence of aggregation and deposition growth. The contributions of St regions to the growth of D_m and IWC in the clouds were 80% and 88% respectively for the shallow events, with 86% and 91% respectively for the deep events. The results indicated that the growth of particle size and mass mainly occurred in the St regions, which corresponded well with the previous studies (e.g., Matejka et al. 1980; Houze et al. 1981; Plummer et al. 2015).

(4) For all events, the medians of N, D_m, and IWC inside GCs were greater than those outside GCs. The average ratios of the median N, D_m, and IWC inside GCs to those outside GCs are 2, 1.3, and 2.5 respectively for the shallow events, with 1.7, 1.2, and 2.3 respectively for the deep events. The upward air motions inside GCs bring more water vapor for ice growth and enhances the activated rate of ice nuclei, which may be a reason for the larger values of N, D_m, and IWC inside GCs.

(5) For all events, the medians of N, D_m, and IWC inside FSs were greater than those outside FSs. The average ratios of the median N, D_m, and IWC inside FSs to those outside FSs are 2, 1.4, and 2.5 respectively for the shallow events, with 1.7, 1.3, and 2.3 respectively for the deep events, which were basically the same as the average ratios for the GC regions. Since there was no apparent difference in W_a inside and outside the FSs, the results implied the importance of GCs to the enhanced ice growth subsequently found in FSs, which correspond well with the previous studies (Plummer et al. 2014; Plummer et al. 2015).

(6) In this study, 1988571 effective data points were fitted to establish the first Z_e–

IWC relationship suitable for snow clouds in the midlatitudes of China, and the relationship was compared with the others in the relevant literature. The purpose of this study is to test the feasibility of calculating IWC through the Z_e observed by ground-based CVPR-FMCW, rather than establishing a universally applicable formula about snowfall remote sensing.

In this study, the N, D_m and IWC values were retrieved more precisely by using Doppler spectra from CVPR-FMCW. The aim was to obtain a relatively continuous and complete understanding of the distribution of N, D_m, and IWC in the GC and St regions during shallow and deep events. Furthermore, the differences in N, D_m, and IWC between the inside and outside of GCs and FSs were also discussed associated with the dynamical properties. Finally, the first Z_e–IWC relationship suitable for snow clouds in the midlatitudes of China was established, and the possibility of studying IWC in snow clouds through Z_e observed by ground-based radar was discovered. The Z_e–IWC relationships for different regions and different types of snow events will be established and compared in the future work.

Acknowledgment

This work has been supported by the National Key Research and Development Program of China under Grant 2017YFC1501703，National Natural Science Foundation of China (41675029，41975046), research project of State Key Laboratory of Severe Weather (LaSW). We would like to thank LetPub (www.letpub.com) for providing linguistic assistance during the preparation of this manuscript.

References

American Meteorological Society, 2016: Generating cell. Glossary of Meteorology. [Available online at http://glossary.ametsoc.org/wiki/Generating_cell].

Bailey, M. P., and J. Hallett, 2009: A comprehensive habit diagram for atmospheric ice crystals: Confirmation from the laboratory, AIRS II, and other field studies. J. Atmos. Sci., 66, 2888–2899, doi:10.1175/2009JAS2883.1.

Boucher, R. J., 1959: Synoptic-physical implications of 1.25-cm vertical-beam radar echoes. J. Meteor., 16, 312–326, doi:10.1175/1520-0469(1959)016,0312:SPIOCV.2.0.CO;2.

Bringi, V. N., L. Tolstoy, M. Thurai, and W. A. Petersen, 2015: Estimation of spatial correlation of drop size distribution parameters and rain rate using NASA's S-band polarimetric radar and 2D video disdrometer network: Two case studies from MC3E. J. Hydrometeor., 16, 1207–1221, doi:10.1175/JHM-D-14-0204.1.

Carbone, R. E., and A. R. Bohne, 1975: Cellular snow generation—A Doppler radar study. J. Atmos. Sci., 32, 1384–1394, doi:10.1175/1520-0469(1975)032,1384:CSGDRS.2.0.CO;2.

Connolly, P. J., C. Emersic, and P. R. Field, 2012: A laboratory investigation into the aggregation efficiency of small ice crystals. Atmos. Chem. Phys., 12, 2055–2076, doi:10.5194/acp-12-2055-2012.

Crosier, J., and Coauthors, 2014: Microphysical properties of cold frontal rainbands. Quart. J. Roy. Meteor. Soc., 140, 1257–1268, doi:10.1002/qj.2206.

Cui, Y., Z. Ruan, M. Wei, F. Li, and R. Ge, 2020: Vertical structure and dynamical properties during snow events in middle latitudes of China from observations by the C-band vertically pointing radar. J. Meteor. Soc. Japan, 98, 527–550, doi:10.2151/jmsj.2020-028.

Cunningham, J. G., and S. E. Yuter, 2014: Instability characteristics of radar-derived mesoscale organization modes within coolseason precipitation near Portland, Oregon. Mon. Wea. Rev., 142, 1738–1757, doi:10.1175/MWR-D-13-00133.1.

Dawson, D. T., E. R. Mansell, and M. R. Kumjian, 2015: Does Wind Shear Cause Hydrometeor Size Sorting? J. Atmos. Sci., 72, 340–348, doi:10.1175/JAS-D-14-0084.1.

Delanoë, J., A. Protat, D. Bouniol, A. Heymsfield, A. Bansemer, and P. Brown, 2007: The characterization of ice cloud properties from Doppler radar measurements. J. Appl. Meteor. Climatol., 46, 1682–1698, doi:10.1175/JAM2543.1.

Douglas, R. H., K. L. S. Gunn, and J. S. Marshall, 1957: Pattern in the vertical of snow generation. J. Meteor. 14, 95–114, doi:10.1175/1520-0469(1957)014<0095:PITVOS>2.0.CO;2.

Draine, B. T., and P. J. Flatau, 1994: Discrete-dipole approximation for scattering calculations. J. Opt. Soc. Amer. A, 11, 1491, doi:10.1364/JOSAA.11.001491.

Gunn, K. L. S., M. P. Langleben, A. S. Dennis, and B. A. Power, 1954: Radar evidence of a generating level for snow. J. Meteor. 11, 20–26, doi:10.1175/1520-0469(1954)011<0020:REOAGL>2.0.CO;2.

Henrion, X., H. Sauvageot, and D. Ramond, 1978: Finestructure of precipitation and temperature in a stratocumulus cloud. J. Atmos. Sci., 35, 2315–2324, doi:10.1175/1520-0469(1978)035,2315:FOPATI.2.0.CO;2.

Herzegh, P. H., and P. V. Hobbs, 1980: The mesoscale and microscale structure and organization of clouds and precipitation in mid-latitude cyclones. II: Warm-frontal clouds. J. Atmos. Sci., 37, 597–611, doi:10.1175/1520-0469(1980)037,0597:TMAMSA.2.0.CO;2.

Heymsfield, A. J., Z. Wang, and S. Matrosov, 2005: Improved radar ice water content retrieval algorithms using coincident microphysical and radar measurements. J. Appl. Meteor., 44, 1391–1412, doi:10.1175/JAM2282.1.

Heymsfield, A. J., and C. D. Westbrook, 2010: Advances in the estimation of ice particle fall speeds using laboratory and field measurements. J. Atmos. Sci., 67, 2469–2482, doi:10.1175/2010JAS3379.1.

Heymsfield, A. J., C. Schmitt, and A. Bansemer, 2013: Ice cloud particle size distributions and pressure-dependent terminal velocities from in situ observations at temperatures from 0° to −86°C. J. Atmos. Sci., 70, 4123–4154, doi:10.1175/JAS-D-12-0124.1.

Heymsfield, A., and P. Willis, 2014: Cloud conditions favoring secondary ice particle production in tropical maritime convection. J. Atmos. Sci., 71, 4500–4526.

Heymsfield, A. J., S. Y. Matrosov, and N. B. Wood, 2016: Toward Improving Ice Water Content and Snow-Rate Retrievals from Radars. Part I: X and W Bands, Emphasizing CloudSat. J. Appl. Meteor. Climatol., 55, 2063–2090, doi:10.1175/JAMC-D-15-0290.1.

Hobbs, P. V., and J. D. Locatelli, 1978: Rainbands, precipitation cores and generating cells in a cyclonic storm. J. Atmos. Sci., 35, 230–241, doi:10.1175/1520-0469(1978)035,0230:RPCAGC.2.0.CO;2.

Hogan, R. J., M. P. Mittermaier, and A. J. Illingworth, 2006: The retrieval of ice water content from radar reflectivity factor and temperature and its use in evaluating a mesoscale model. J. Appl. Meteor. Climatol., 45, 301–317, doi:10.1175/JAM2340.1.

Hogan, R. J., and C. D. Westbrook, 2014: Equation for the microwave backscatter cross section of aggregate snowflakes using the self-similar Rayleigh–Gans approximation. J. Atmos. Sci., 71, 3292–3301, doi:10.1175/JAS-D-13-0347.1.

Houze, R. A., Jr., S. A. Rutledge, T. J. Matejka, and P. V. Hobbs, 1981: The mesoscale and microscale structure and organization of clouds and precipitation in midlatitude cyclones. III: Air motions and precipitation growth in a warm-frontal rainband. J. Atmos. Sci. 38, 639–649, doi:10.1175/1520-0469(1981)038,0639:TMAMSA.2.0.CO;2.

Kajikawa, M., 1982: Observation of the falling motion of early snow flakes. Part I: Relationship between the free-fall pattern and the number and shape of component snow crystals. J. Meteor. Soc. Japan, 60, 797–803.

Kalesse, H., P. Kollias, and W. Szyrmer, 2013: On using the relationship between Doppler velocity and radar reflectivity to identify microphysical processes in midlatitudinal ice clouds. J. Geophys. Res. Atmos., 118, 12168–12179, doi:10.1002/2013JD020386.

Keppas, S. Ch., J. Crosier, T. W. Choularton and K. N. Bower, 2018: Microphysical properties and radar polarimetric features within a warm front. Mon. Wea. Rev., 146, 2003–2022. doi:10.1175/MWR-D-18-0056.1.

Kumjian, M. R., and A. V. Ryzhkov, 2012: The impact of size sorting on the polarimetric radar variables. J. Atmos. Sci., 69, 2042–2060, doi:10.1175/JAS-D-11-0125.1.

Kumjian, M. R., S. A. Rutledge, R. M. Rasmussen, P. C. Kennedy, and M. Dixon, 2014: High-resolution polarimetric radar observations of snow-generating cells. J. Appl. Meteor. Climatol., 53, 1636–1658. doi:10.1175/JAMC-D-13-0312.1.

Laksmono, H., T. A. McQueen, J. A. Sellberg, N. D. Loh, C. Huang, D. Schlesinger, R. G. Sierra, C. Y. Hampton, et al., 2015: Anomalous behavior of the homogeneous ice nucleation rate in “No-Man’s Land”. J. Phys. Chem. Lett., 6, 2826−2832. doi:10.1021/acs.jpclett.5b01164.

Langleben, M. P., 1956: The plan pattern of snow echoes at the generating level. J. Meteor. 13, 554–560.

Locatelli, J. D., and P. V. Hobbs, 1974: Fall speeds and masses of solid precipitation particles. J. Geophys. Res., 79, 2185–2197.

Lu, Y., Z. Jiang, K. Aydin, J. Verlinde, E. E. Clothiaux, and G. Botta, 2016: A polarimetric scattering database for non-spherical ice particles at microwave wavelengths. Atmos. Meas. Tech., 9, 5119–5134, doi:10.5194/amt-9-5119-2016.

Mackowski, D. W. and M. I. Mishchenko, 1996: Calculation of the T matrix and the scattering matrix for ensembles of spheres, J. Opt. Soc. Amer. A, 13, 2266–2278.

Marshall, J. S., 1953: Precipitation trajectories and patterns. J. Atmos. Sci. 10, 25–29, doi:10.1175/1520-0469(1953)010<0025:PTAP>2.0.CO;2.

Matejka, T. J., R. A. Houze Jr., and P. V. Hobbs, 1980: Microphysics and dynamics of clouds associated with mesoscale rainbands in extratropical cyclones. Quart. J. Roy. Meteor. Soc., 106, 29–56, doi:10.1002/qj.49710644704.

Matrosov, S. Y., 1992: Radar reflectivity in snowfall. IEEE Trans. Geosci. Remote Sens., 30, 454–461, doi:10.1109/36.142923.

Matrosov, S. Y., and A. J. Heymsfield, 2000: Use of Doppler radar to assess ice cloud particle fall velocity–size relations for remote sensing and climate studies. J. Geophys. Res., 105, 22427–22436.

McFarquhar, G. M., and Coauthors, 2011: Indirect and semi-direct aerosol campaign. Bull. Amer. Meteor. Soc., 92, 183–201, doi:10.1175/2010BAMS2935.1.

Mitchell, D. L., 1996: Use of mass- and area-dimensional power laws for determining precipitation particle terminal velocities. J. Atmos. Sci., 53, 1710–1723.

Mossop, S. C., 1976: Production of secondary ice particles during growth of graupel by riming. Quart. J. Roy. Meteor. Soc., 102, 45–57.

Plummer, D. M., G. M. McFarquhar, R. M. Rauber, B. F. Jewett, and D. C. Leon, 2014: Structure and statistical analysis of the microphysical properties of generating cells in the comma head region of continental winter cyclones. J. Atmos. Sci. 71, 4181–4203, doi:10.1175/JAS-D-14-0100.1.

Plummer, D. M., G. M. McFarquhar, R. M. Rauber, B. F. Jewett, and D. C. Leon, 2015: Microphysical properties of convectively generated fall streaks within the stratiform comma head region of continental winter cyclones. J. Atmos. Sci. 72, 2465–2483, doi:10.1175/JAS-D-14-0354.1.

Protat, A., J. Delanoë, D. Bouniol, A. J. Heymsfield, A. Bansemer, and P. Brown, 2007: Evaluation of ice water content retrievals from cloud radar reflectivity and temperature using a large airborne in situ microphysical database. J. Appl. Meteor. Climatol., 46, 557–572, doi:10.1175/JAM2488.1.

Protat, A., and C. R. Williams, 2011: The accuracy of radar estimates of ice terminal fall speed from vertically pointing Doppler radar measurements. J. Appl. Meteor. Climatol., 50, 2120–2138, doi:10.1175/JAMC-D-10-05031.1.

Ralph, F. M., 1995: Using radar-measured radial vertical velocities to distinguish precipitation scattering from clear-air scattering. J. Atmos. Oceanic Technol., 12, 257–267, doi:10.1175/1520-0426(1995)012,0257:URMRVV.2.0.CO;2.

Rauber, R. M., S. M. Ellis, J. Vivekanandan, J. Stith, W.-C. Lee, G. M. McFarquhar, B. F. Jewett, and A. Janiszeski, 2017: Finescale structures of a snowstorm over the northeastern United States: A first look at high-resolution HIAPER Cloud Radar observations. Bull. Amer. Meteor. Soc., 98, 253–269, doi:10.1175/BAMS-D-15-00180.1.

Rosenow, A. A., D. M. Plummer, R. M. Rauber, G. M. McFarquhar, B. F. Jewett, and D. Leon, 2014: Vertical velocity and physical structure of generating cells and convection in the comma head region of continental winter cyclones. J. Atmos. Sci. 71, 1538–1558, doi:10.1175/JAS-D-13-0249.1.

Rutledge, S. A., and P. V. Hobbs, 1983: The mesoscale and microscale structure and organization of clouds and precipitation in midlatitude cyclones. VIII: A model for the "seeder-feeder" process in warm-frontal rainbands. J. Atmos. Sci., 40, 1185–1206, doi:10.1175/1520-0469(1983)040,1185:TMAMSA.2.0.CO;2.

Sekhon, R. S., and R. C. Srivastava, 1970: Snow size spectra and radar reflectivity. J. Atmos. Sci., 27, 299–307.

Schmitt, C. G., and A. J. Heymsfield, 2014: Observational quantification of the separation of simple and complex atmospheric ice particles. Geophys. Res. Lett., 41, 1301–1307, doi:10.1002/2013GL058781.

Shupe, M. D., P. Kollias, S. Y. Matrosov, T. L. Schneider, 2008: On Deriving Vertical Air Motions from Cloud Radar Doppler Spectra. J. Atmos. Ocean. Technol., 25, 547–557.

Sienkiewicz, J. M., J. D. Locatelli, P. V. Hobbs, and B. Geerts, 1989: Organization and structure of clouds and precipitation on the mid-Atlantic coast of the United States. Part II: The mesoscale and microscale structures of some frontal rainbands. J. Atmos. Sci., 46, 1349–1364.

Straka, J., Zrnic, D. S., and Ryzhkov, A. V. (2000). Bulk hydrometeor classification and quantification using polarimetric radar data: Synthesis of relations. J. Appl. Meteor., 39, 1341–1372. doi:10.1175/1520-0450(2000)039%3C1341:BHCAQU%3E2.0.CO;2.

Syrett, W. J., B. A. Albrecht, and E. E. Clothiaux, 1995: Vertical cloud structure in a midlatitude cyclone from a 94-GHz radar. Mon. Wea. Rev., 123, 3393–3407, doi:10.1175/1520-0493(1995)123,3393:VCSIAM.2.0.CO;2.

Testud, J., S. Oury,R. A. Black, P. Amayenc, and X.K. Dou, 2001: The concept of "normalized" distribution to describe raindrop spectra: A tool for cloud physics and cloud remote sensing. J. Appl. Meteor., 40, 1118–1140, doi:10.1175/1520-0450(2001)040,1118:TCONDT.2.0.CO;2.

Thomason, J., A. Illingworth, and V. Marecal, 1995: Density and size distribution of aggregating snow particles inferred from coincident aircraft and radar observations. Preprints, 27th Conf. on Radar Meteorology, Vail, CO, Amer. Meteor. Soc., 127–129.

Tyynelä, J., J. Leinonen, C. D. Westbrook, D. Moisseev, and T. Nousiainen, 2013: Applicability of the Rayleigh-Gans approximation for scattering by snowflakes at microwave frequencies in vertical incidence. J. Geophys. Res. Atmos., 118, 1826–1839, doi:10.1002/jgrd.50167.

Ulbrich, C. W., 1983: Natural variations in the analytical form of the raindrop size distribution. J. Climate Appl. Meteor., 22, 1764–1775.

van de Hulst, H. D., 1957: Light Scattering by Small Particles. Wiley and Sons, 470 pp.

Welti, A., Z. A. Kanji, O. Stetzer, U. Lohmann, and F. Lüönd, 2014: Exploring the mechanisms of ice nucleation on kaolinite: From deposition nucleation to condensation freezing. J. Atmos. Sci. 71, 16–36, doi:10.1175/JAS-D-12-0252.1.

Westbrook, C. D., R. C. Ball, and P. R. Field, 2006: Radar scattering by aggregate snowflakes. Quart. J. Roy. Meteor. Soc., 132, 897–914, doi:10.1256/qj.05.82.

Wexler, R., 1955: Radar analysis of precipitation streamers observed 25 February 1954. J. Atmos. Sci. 12, 391–393, doi:10.1175/1520-0469(1955)012<0391:RAOPSO>2.0.CO;2.

Wexler, R., and D. Atlas, 1959: Precipitation generating cells. J. Atmos. Sci., 16, 327–332, doi:10.1175/1520-0469(1959)016,0327:PGC.2.0.CO;2.

Williams, C. R., 2016: Reflectivity and liquid water content vertical decomposition diagrams to diagnose vertical evolution of raindrop size distributions. J. Atmos. Oceanic Technol., 33, 579–595, doi:10.1175/JTECH-D-15-0208.1.

Wolde, M., and G. Vali, 2002: Cloud structure and crystal growth in nimbostratus. Atmos. Res., 61, 49–74, doi:10.1016/S0169-8095(01)00102-8.

Yuter, S. E., and R. A. Houze, 1995: Three-dimensional kinematic and microphysical evolution of Florida cumulonimbus. Part II: Frequency distributions of vertical velocity, reflectivity, and differential reflectivity. Mon. Wea. Rev., 123, 1941–1963, doi:10.1175/1520-0493(1995)123,1941:TDKAME.2.0.CO;2.

Zawadzki, I., F. Fabry, and W. Szyrmer, 2001: Observations of supercooled water and secondary ice generation by a vertically pointing X-band Doppler radar. Atmos. Res., 59–60, 343–359, doi:10.1016/S0169-8095(01)00124-7.